



OPEN ACCESS

EDITED BY

Bayarto Lubsandorzhev,
Institute for Nuclear Research (RAS),
Russia

REVIEWED BY

Atanu Pathak,
Purdue University Northwest,
United States
Ivashkin Alexander,
Institute for Nuclear Research (RAS),
Russia

*CORRESPONDENCE

A. Razeto,
razeto@infn.it

RECEIVED 07 March 2023

ACCEPTED 24 April 2023

PUBLISHED 16 May 2023

CITATION

Boulay MG, Camillo V, Canci N,
Choudhary S, Consiglio L, Flammini A,
Galbiati C, Ghiano C, Gola A, Horikawa S,
Kachru P, Kochanek I, Kondo K, Korga G,
Kuźniak M, Mazzi A, Moharana A,
Nieradka G, Paternoster G, Razeto A,
Sablone D, Thorpe TN, Türkoğlu C,
Wang H, Rescigno M and Sanfilippo S
(2023), SiPM cross-talk in liquid
argon detectors.
Front. Phys. 11:1181400.
doi: 10.3389/fphy.2023.1181400

COPYRIGHT

© 2023 Boulay, Camillo, Canci,
Choudhary, Consiglio, Flammini,
Galbiati, Ghiano, Gola, Horikawa,
Kachru, Kochanek, Kondo, Korga,
Kuźniak, Mazzi, Moharana,
Nieradka, Paternoster, Razeto,
Sablone, Thorpe, Türkoğlu, Wang,
Rescigno and Sanfilippo. This is an
open-access article distributed under
the terms of the [Creative Commons Attribution
License \(CC BY\)](https://creativecommons.org/licenses/by/4.0/). The use, distribution
or reproduction in other forums is
permitted, provided the original author(s)
and the copyright owner(s) are credited
and that the original publication in this
journal is cited, in accordance with
accepted academic practice. No use,
distribution or reproduction is permitted
which does not comply with these terms.

SiPM cross-talk in liquid argon detectors

M. G. Boulay^{1,2}, V. Camillo¹, N. Canci¹, S. Choudhary³,
L. Consiglio¹, A. Flammini⁴, C. Galbiati^{5,6}, C. Ghiano¹, A. Gola^{7,8},
S. Horikawa⁵, P. Kachru⁵, I. Kochanek¹, K. Kondo¹, G. Korga⁹,
M. Kuźniak³, A. Mazzi^{7,8}, A. Moharana⁵, G. Nieradka³,
G. Paternoster^{7,8}, A. Razeto^{1*}, D. Sablone¹, T. N. Thorpe^{5,10},
C. Türkoğlu³, H. Wang¹⁰, M. Rescigno¹¹ and S. Sanfilippo¹²

¹INFN Laboratori Nazionali del Gran Sasso, L'Aquila, Italy, ²Department of Physics, Carleton University, Ottawa, ON, Canada, ³AstroCeNT, Nicolaus Copernicus Astronomical Center of the Polish Academy of Sciences, Warsaw, Poland, ⁴INFN Bologna, Bologna, Italy, ⁵Gran Sasso Science Institute, L'Aquila, Italy, ⁶Physics Department, Princeton University, Princeton, NJ, United States, ⁷Fondazione Bruno Kessler, Povo, Italy, ⁸Trento Institute for Fundamental Physics and Applications, Povo, Italy, ⁹Department of Physics, Royal Holloway University of London, Egham, United Kingdom, ¹⁰Physics and Astronomy Department, University of California, Los Angeles, CA, United States, ¹¹INFN Sezione di Roma, Roma, Italy, ¹²INFN Roma Tre, Roma, Italy

SiPM-based readouts are becoming the standard for light detection in particle detectors given their superior resolution and ease of use with respect to vacuum tube photo-multipliers. However, the contributions of noise detection such as the dark rate, cross-talk, and after-pulsing (AP) may significantly impact their performance. In this work, we present the development of highly reflective single-phase argon chambers capable of displaying light yields up to 32 photo-electrons per keV, with approximately 12 being primary photo-electrons generated by the argon scintillation, while the rest are accounted by optical cross-talk. Furthermore, the presence of compound processes results in a generalized Fano factor larger than 2 already at an over-voltage of 5 V. Finally, we present a parametrization of the optical cross-talk for the FBK NUV-HD-Cryo SiPMs at 87 K that can be extended to future detectors with tailored optical simulations.

KEYWORDS

liquid argon detector, light yield, SiPM, cross-talk, correlated noises

1 Introduction

In 1955, it was observed that a silicon junction emits light when a bias is applied across it [1]. More recently, a number of works have documented the emission of light by SiPMs during the avalanche process [2–5]. Internal cross-talk (iCT) happens when such a photon remains confined within the source SiPM and generates another avalanche in a neighboring cell. External cross-talk (eCT) happens when the generated photon escapes from the silicon bulk reaching another SiPM array in the experimental setup. Lastly, feedback cross-talk (fCT) happens when the photon undergoes reflection and is reabsorbed by the same SiPM array which emitted it. We define optical cross-talk (oCT) as the envelope that includes all three of these effects. As we will describe, optical cross-talk generates a compound process that leads to the amplification of the number of detected photo-electrons $\mathcal{A}^{\text{pe}} = 1/(1 - \lambda_{\text{oCT}})$ (where $\lambda_{\text{oCT}} \ll 1$ is the average number of secondary avalanches following any avalanche in the process). Unfortunately, such processes are subjected to fluctuations that affect the

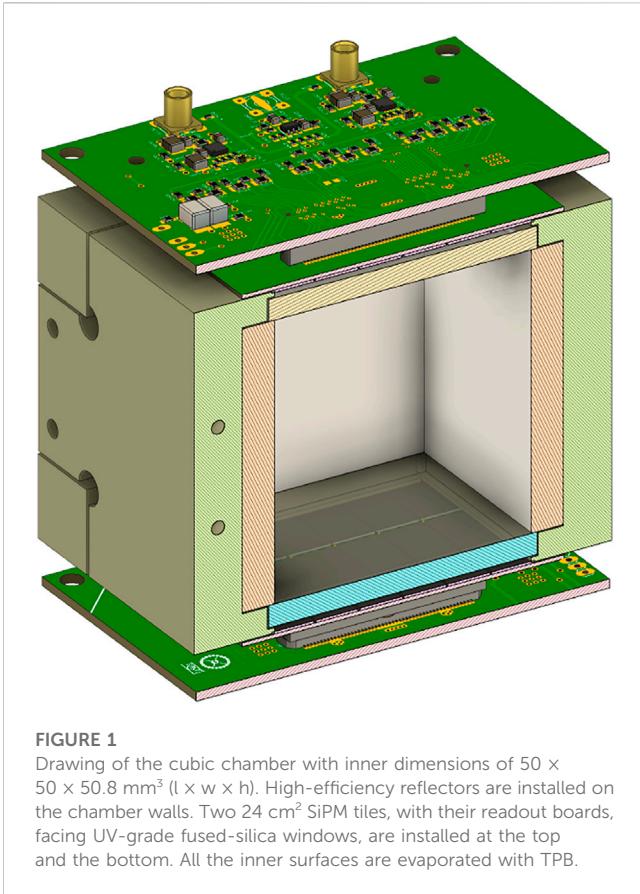


FIGURE 1

Drawing of the cubic chamber with inner dimensions of $50 \times 50 \times 50.8 \text{ mm}^3$ ($l \times w \times h$). High-efficiency reflectors are installed on the chamber walls. Two 24 cm^2 SiPM tiles, with their readout boards, facing UV-grade fused-silica windows, are installed at the top and the bottom. All the inner surfaces are evaporated with TPB.

resolution of the measurement. This is addressed in Section 3.5, where we quantify a generalized Fano factor that is significantly larger than unity.

Many particle detectors are designed to collect very faint light signals in chambers that host several thousands of photo-detectors, such as Borexino and Super-Kamiokande [6, 7]. Under these conditions, oCT between the photo-detectors can have a large impact on the physics results of the experiments. Argon is of particular interest as an active detector medium because of its high scintillation yield. Multiple large particle detectors have made, or will make, use of liquid argon (LAr) [8–11]. In this work, we present the development of two high-efficiency LAr chambers which were operated at 87 K to study the scintillation light produced by the interactions with calibration sources. We then present the deconvolution of the oCT into the individual contributions.

2 Experimental setups

The detectors were installed in a sealed dewar inside a container filled with approximately 4 L of high-purity LAr, within the STAR facility [12]. The system consists of a re-circulation loop with a volumetric flow of 5 sL/min and provides continuously purified argon via a getter (SAES PS4-MT3).

Two radioactive sources were used. The meta-stable isotope, $^{83\text{m}}\text{Kr}$, with an activity of $\mathcal{O}(10)$ Bq, was injected into the re-

circulation loop. $^{83\text{m}}\text{Kr}$ has been used in previous direct dark matter experiments [13], as it is not filtered by the getters, and provides a calibration line at 41.5 keV. ^{241}Am can be attached to the external wall of the dewar, providing 59.5 keV gamma rays within the active volume of the detector at a rate of several Hertz.

2.1 Cubic chamber

Figure 1 depicts the cubic LAr chamber. The chamber consists of four identical walls machined from polyetheretherketone (PEEK) which can host different reflectors. The results reported here refer to an enhanced specular reflector (Vikuiti ESR) from 3M company. The top and bottom windows are made of 1λ fused silica with dimensions of $50 \times 50 \times 4 \text{ mm}^3$. All internal surfaces are coated with tetraphenyl butadiene (TPB) for the wavelength shifting of the scintillation photons (128 nm) to the visible range of the spectrum.

The visible photons are detected by two SiPM arrays (tiles) installed at the top and bottom of the detector chamber. Each tile consists of 24 SiPMs (summed into quadrants) bonded to a FR4 PCB with cryo-grade epoxy [14]. The SiPMs of the FBK NUV-HD-Cryo family have a surface area of $7.9 \times 11.7 \text{ mm}^2$, with a cell size of $30 \mu\text{m}$ and a quenching resistor of $5 \text{ M}\Omega$ at 87 K [15]. The fill-factor of the tiles is 90%, where most of the dead space is reserved for the landing pad of the wire bonding.

2.2 Cylindrical chamber

A cylindrical chamber with inner dimensions of $46 \times 50 \text{ mm}^2$ ($\phi \times h$) is instrumented with the same photo-detectors as used in the cubic chamber. The cylinder is made of acrylic and internally lined with TPB-coated 3M reflector foil. In front of the SiPM surface, two 1-mm-thick TPB-coated fused-silica windows are installed. The cylindrical chamber is used for verifying the consistency of the results and the models developed for the cubic chamber.

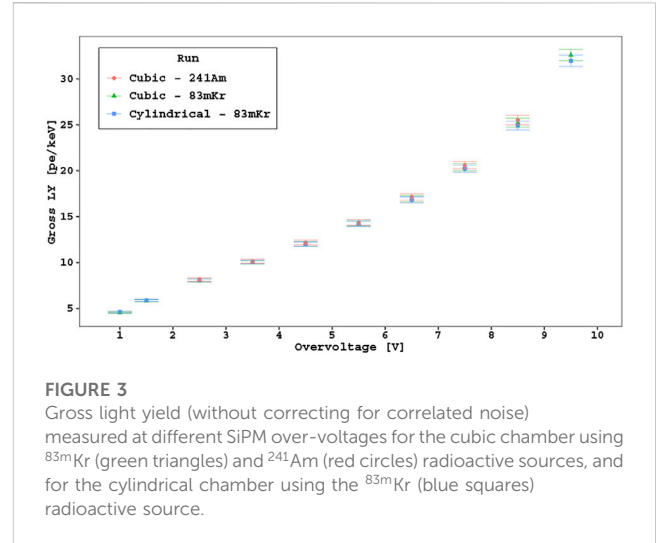
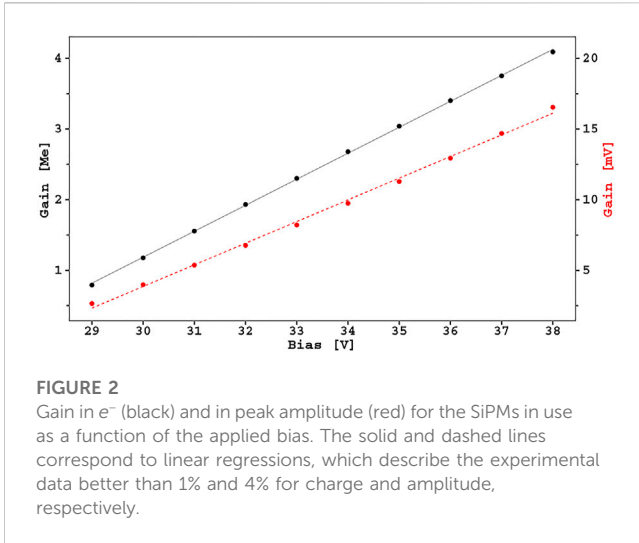
2.3 Data acquisition

Each tile is connected to a readout board where the signals from the SiPMs are amplified by four cryo-grade low-noise trans-impedance amplifiers [16]. In this configuration, we achieve at an over-voltage (σV) of 5 V a signal-to-noise ratio¹ (SNR) larger than 7 for the unfiltered signal and larger than 30 for the charge in $1 \mu\text{s}$.

Waveforms are acquired using a V1720 CAEN digitizer, with each tile quadrant connected to a channel. A copy of the signal from the SiPMs is sent to a set of NIM discriminators that form a trigger logic unit. The trigger can be configured to act on a single tile or on both, depending on the experimental conditions. The trigger threshold is set significantly below the region of interest.

Data are acquired up to an over-voltage of 9.5 V with ^{241}Am , $^{83\text{m}}\text{Kr}$, and with no radioactive source present. The latest

¹ The SNR is defined as an average signal for the single photo-electron over the baseline noise at one sigma, both under the same filtering condition.



configuration is useful to subtract the background spectrum from the source data obtaining the clean energy peaks [12].

A laser pulse is delivered in the chambers to monitor the behavior of the photo-detectors. Figure 2 shows the charge gain and the peak amplitude for one of the SiPMs in use. Both quantities are described being better than a few percent by linear models (as a function of over-voltage). The break-down voltages are measured as $V_{bd}^C = (26.8 \pm 0.1)$ V and $V_{bd}^A = (27.5 \pm 0.1)$ V for charge and amplitude, respectively. Here, the over-voltage is relative to V_{bd}^A .

3 Data analysis

The data analysis involves integrating the normalized waveforms over a gate of $7 \mu\text{s}$, following the NIM trigger to obtain the photo-electron (PE) spectrum. Over this time scale, 99.5% of the Ar scintillation light is emitted [17], and delays introduced by the absorption and re-emission of photons in the wavelength shifter (WLS) and their optical path length inside the detector are slightly affected. The normalized waveforms are scaled by the gain of the photo-detectors, and the baseline, which is calculated in the pre-trigger region, is removed. The mean number of photo-electrons observed by both photo-detectors is extracted by fitting the calibration peak data with a Gaussian model [12].

The gross light yield, LY_G^{oV} , is the ratio of the number of detected photo-electrons to the energy deposited within the medium by the radioactive source. The gross energy resolution, σ_G^{oV}/E , is determined by the standard deviation divided by the mean of the fitted Gaussian model. Figure 3 shows LY_G^{oV} versus over-voltage for the cubical and the cylindrical chambers, where similar values are obtained for both radioactive sources.

3.1 Internal cross-talk and after-pulsing

Figure 4 shows two figures of merit for the iCT for the SiPMs in use, measured at 77 K. These measurements are performed with

single SiPMs from the same lot as the photo-detectors of the cylindrical and cubic chambers. The SiPMs are exposed to laser pulses in a stable, low-noise environment, with a black masking tape to minimize the contribution of external photons and feedback cross-talk. During analysis, up to 20 photo-electron peaks are identified. We can assume that the number of detected laser photons follow a Poissonian distribution with a mean value, e^{oV} (taken much smaller than unity).

In this work, we assume that the cross-talk photons are emitted independently in a recursive process converging at $e^{oV}/(1 - \lambda_{iCT})$, where λ_{iCT} is the average number of secondary avalanches following any avalanche in the process. As in Ref. [18], the model is valid for $\lambda_{iCT} \ll 1$.

Using the charge spectra (aka “finger plots”), the relative population of each peak, \mathcal{R}_n^{oV} (relative to n photo-electrons), is extracted. Using the properties of the Poissonian distribution for laser photo-electrons, the following quantities are defined:

$$\begin{aligned} e^{oV} &= -\ln(\mathcal{R}_0^{oV}), \\ \lambda_{iCT}^{oV} &= 1 - \frac{e^{oV}}{\langle n \rangle}, \\ \mathcal{F}_{iCT}^{oV} &= \frac{\text{Var}[n]}{\langle n \rangle}, \end{aligned} \tag{1}$$

where $\text{Var}[n]$ and $\langle n \rangle$ define the variance and mean of the photo-electron peak distribution, (\mathcal{R}_n^{oV}) , respectively. Equation 1 provides the maximum likelihood estimates for λ_{iCT} and the generalized Fano factor (\mathcal{F}_{iCT}) with the experimental data, which are shown as green points in Figure 4.

The generalized Fano factor (\mathcal{F}_{iCT}) is defined as a simple variance-to-mean ratio and quantifies the deviation from the Poisson model. If the primary photo-electrons follow a Poisson distribution, the generalized Fano factor is related to the excess noise factor (ENF) as $\mathcal{F} = \mathcal{A} \cdot \text{ENF}$, where \mathcal{A} is the amplification factor. In our setup, such amplification is provided by the iCT; therefore, $\mathcal{A} = \mathcal{A}^{\text{pe}}$.

We model the behavior of λ_{iCT}^{oV} and \mathcal{F}_{iCT}^{oV} with the following equations:

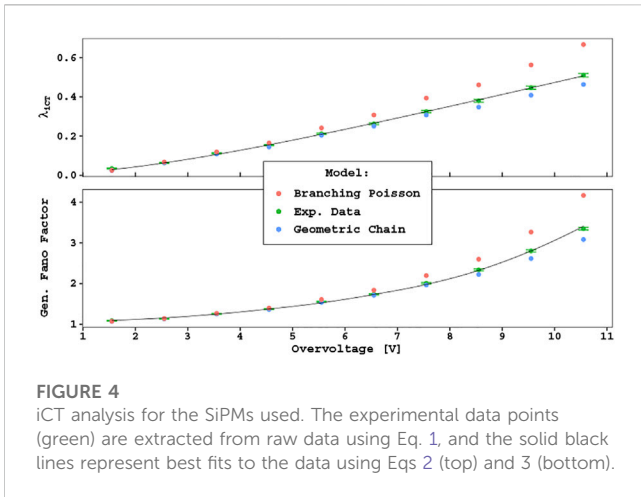


FIGURE 4
iCT analysis for the SiPMs used. The experimental data points (green) are extracted from raw data using Eq. 1, and the solid black lines represent best fits to the data using Eqs 2 (top) and 3 (bottom).

$$\lambda_{iCT}(V) = \xi_{iCT} \cdot (V - V_{bd}^C) \cdot P_T^h(V - V_{bd}^A), \quad (2)$$

$$\mathcal{F}_{iCT}(V) = \delta \cdot (1 - \lambda_{iCT}(V))^\alpha, \quad (3)$$

where the two break-down voltages (V_{bd}^A and V_{bd}^C) are determined by the laser data analysis described in Section 2.3.

Equation 2 describes the iCT process in terms of emission and trigger probabilities [19]. The iCT photons are peaked in the red–infrared region [2], where the detection of the NUV SiPMs is carried out by holes. Therefore, in Eq. 2, only the hole triggering probability (P_T^h) is used. The emission probability is considered to be proportional to the total number of carriers extracted in the avalanche process, which is directly proportional to $V - V_{bd}^C$ (at better than 1%, see Figure 2). The ξ_{iCT} factor represents the acceptance for the iCT process. Equation 3 describes the generalized Fano factor with an effective model depending on two free parameters: α and δ .

The triggering probabilities for hole- and electron-initiated avalanches (P_T^h and P_T^e) are parametrized with exponential dependencies, as shown in Refs [20, 21]. We define

$$\begin{aligned} P_T^h(\Delta V) &= 1 - e^{-\frac{\Delta V}{V_h}}, \\ P_T^e(\Delta V) &= 1 - e^{-\frac{\Delta V}{V_e}}, \end{aligned} \quad (4)$$

where V_h and V_e describe the temperature-dependent mean energy required by a drifting carrier to extract charge with inelastic scattering. We found that the triggering probabilities for our data are better described in terms of $\Delta V = V - V_{bd}^A$ as in Ref. [22], as opposed to Ref. [21] that defines $\Delta V_{Otte} = V - V_{bd}^C$, or to Ref. [23] that defines $\Delta V_{Dinu} = V - V_{bd}^{IV}$ (where V_{bd}^{IV} is the breakdown voltage defined by the I–V curve).

The fits of Eqs 2, 3 converge at $V_h = 5.4(3)$ V and $\xi_{iCT} = (53 \pm 1)$ /kV with $\chi^2/\text{d.o.f.} = 9/8$, and $\alpha = -1.68(1)$ and $\delta = 1.031(8)$ with $\chi^2/\text{d.o.f.} = 13/8$. Figure 4 (solid black lines) shows the prediction of the model using these parameters.

Figure 4 also shows the *branching Poisson* (BP) and *geometric chain* (GC) models as described by Vinogradov [18, 24]. The top panel shows λ_{iCT}^{GC} and λ_{iCT}^{BP} , resulting from the fit of \mathcal{R}_n^{oV} with the corresponding model. The bottom panel shows the generalized Fano factor, which is calculated for GC and BP as $\mathcal{F}_{iCT}^{GC} = (1 + \lambda_{iCT})/(1 - \lambda_{iCT})$ and $\mathcal{F}_{iCT}^{BP} = 1/(1 - \lambda_{iCT})^2$, respectively.

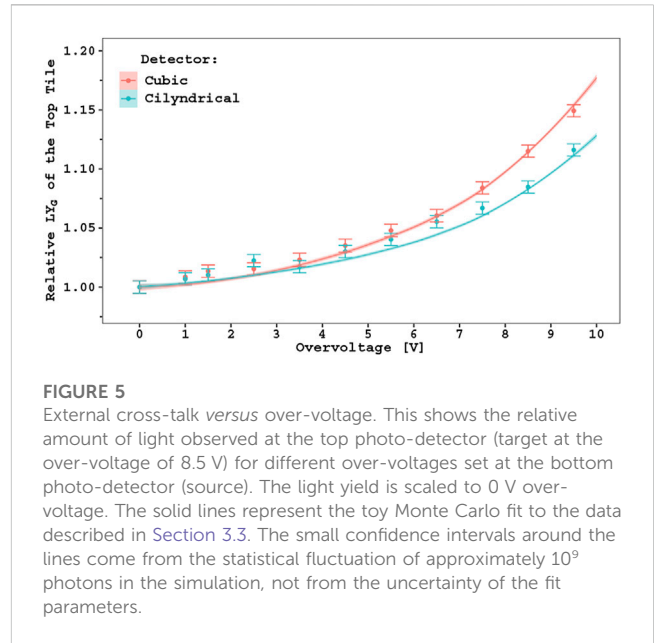


FIGURE 5
External cross-talk versus over-voltage. This shows the relative amount of light observed at the top photo-detector (target at the over-voltage of 8.5 V) for different over-voltages set at the bottom photo-detector (source). The light yield is scaled to 0 V over-voltage. The solid lines represent the toy Monte Carlo fit to the data described in Section 3.3. The small confidence intervals around the lines come from the statistical fluctuation of approximately 10^9 photons in the simulation, not from the uncertainty of the fit parameters.

Both models depart from data by more than 10% at the highest over-voltages. Our data are better modeled by the sum of two binomial processes with probabilities 85% $\cdot \lambda_{iCT}$ and 15% $\cdot \lambda_{iCT}$. In this way, each avalanche can generate 0, 1, or 2 photo-electrons in neighboring cells, where a similar process occurs recursively. The accuracy of this *effective* model is better than 0.2% for the resulting mean number of iCT photo-electrons and their generalized Fano factors.

After-pulsing was studied by Ref. [12], and the over-voltages used here do not exceed 10%. The primary dark rate (DCR) does not exceed 20 cps per photo-sensor under cryogenic conditions. As a first approximation, we do not consider these quantities.

3.2 External cross-talk

The eCT contribution is measured directly by scanning over-voltages with one photo-detector (source) while holding the other (target) at a constant value.

Figure 5 shows the relative increase in LY_G measured by the target versus the over-voltage of the source. In this case, the calibration peak can no longer be modeled as a Gaussian model. The LY_G of the target detector is estimated by the mean of the distribution, with the ^{83m}Kr radioactive source after background subtraction.

With equal tile biases (Figure 3), similar values of LY_G^{oV} are obtained with both chambers; however, the eCT component is found to be lower for the cylindrical chamber. One explanation is the circular cross section of the chamber being approximately two-thirds the area of the SiPM array, with a large fraction of the SiPM surface facing the aluminum support frame, which may result in a larger (smaller) fraction of fCT (eCT).

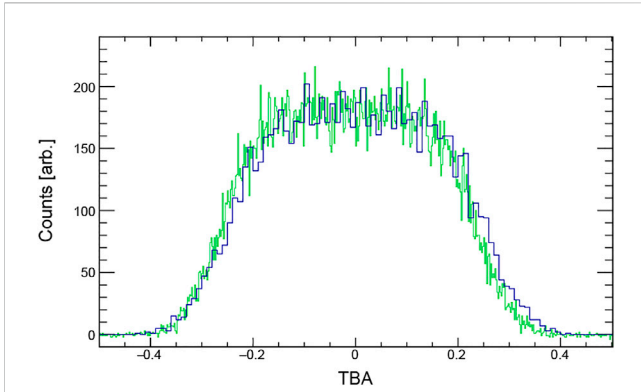


FIGURE 6 Top-bottom asymmetry (TBA) using the ^{83m}Kr radioactive source in the cubic chamber. Experimental data measured at an over-voltage of 8.5 V (green) with an asymmetry below 1.5% and simulated data (blue), which is described in Section 4.

3.3 Toy Monte Carlo simulation

To quantify the different oCT components, a toy Monte Carlo (tMC) simulation is developed. The tMC models the detection of primary photons and the intertwined cross-talk photo-electrons as a recursive binomial process, similar to the geometric compound process from Vinogradov [18] described in Section 3.1. Photon tracking is not part of the tMC, and only the overall acceptances (ξ_x) for each sub-process (primary photo-electrons, iCT, fCT, and eCT) are used.

The tMC assumes a symmetric detector, which is justified by Figure 6, where the top-bottom asymmetry (TBA) is shown for the cubic chamber. The TBA is defined, at the event level, as the difference in photo-electrons observed at the top and bottom

tiles normalized to the total number of collected photo-electrons. Under this hypothesis, the following quantities are defined:

$$P_{\text{PDE}}(V) = \zeta \cdot P_T^e(V - V_{bd}^A) + (1 - \zeta) \cdot P_T^h(V - V_{bd}^A), \quad (5)$$

$$\lambda_{\text{xCT}}(V_S, V_T) = \xi_x \cdot (V_S - V_{bd}^C) \cdot P_T^h(V_T - V_{bd}^A). \quad (6)$$

Equation 5 defines the probability of detecting a primary photon absorbed in the sensitive regions of the SiPM. It is given as the sum of the triggering probabilities, as defined in Eq. 4, weighted for the fraction of the avalanches induced by electrons (ζ) or holes ($1 - \zeta$), see Ref. [22], and asymptotically approaches to unity. The photon-detection efficiency (PDE) can be modeled as $\text{PDE} = a \cdot P_{\text{PDE}}$, with an acceptance coefficient ($a < 1$) that includes the surface reflections and probability of photons materializing outside the sensitive regions. Equation 6 generalizes Eq. 2, modeling the probability of emission and detection of cross-talk photo-electrons as a function of the bias of the source and of the target photo-detectors. For iCT and fCT, V_S and V_T coincide. The acceptance parameters are ξ_{fCT} , ξ_{eCT} , and ξ_{iCT} , the last of which is set to the value obtained from Eq. 2.

χ^2 is minimized by comparing the experimental data of the over-voltage scan against the simulated curves by variation of five free parameters, as shown in Figure 5. The resulting parameters for both the cubic and cylindrical chambers are reported in Table 1. An average accuracy better than 1.5 photo-electrons is achieved, with a relative resolution better than 0.3%.

3.4 Analytical model

An analytical model is independently developed based on simple mathematical assumptions; the tMC helps validate this model. The basic assumption of the model is that the iCT recursive process introduces a photo-electron gain (μ) that can be generalized in the presence of mutually interacting iCT and fCT (described by λ_{iCT} in analogy to λ_{iCT}) as follows:

TABLE 1 Results of the fits to the data for the cubic and the cylindrical chambers. Asymmetric biasing refers to the eCT scan where one photo-detector (target) is kept at constant bias and the other (source) is scanned over the range 0–10 V over-voltage, see Section 3.2. Symmetric biasing corresponds to normal operation where both photo-detectors are held at the same bias. The tMC, the analytical model, and the global fits are reported for the cubic chamber. The parameters without errors are fixed, while V_h (when not fixed) has a penalty in χ^2 at (5.4 ± 0.3) V (see text).

Bias	Cubic			Cylindrical		Unit	
	Asymmetric	Symmetric		Asymmetric	Symmetric		
Algorithm	tMC		Analytical	Global	tMC	Analytical	
\bar{n}^{pe}	13.0 ± 0.5	12.1 ± 0.3	13.0 ± 0.9	12.9 ± 0.9	13.0 ± 0.7	12 ± 2	pe/keV
ζ	0.34 ± 0.05	0.34 ± 0.10	0.34 ± 0.08	0.37 ± 0.08	0.34 ± 0.07	0.45 ± 0.34	—
V_h	5.4	5.4	5.4 ± 0.3	5.6 ± 0.3	5.4	5.3 ± 0.3	V
V_e	1.0 ± 0.1	1.0 ± 0.1	0.9 ± 0.2	1.0 ± 0.2	1	1.1 ± 0.6	V
ξ_{iCT}	53	53	53	53	53	53	kV ⁻¹
ξ_{fCT}	15 ± 1	15	15	15	17 ± 1	17	kV ⁻¹
ξ_{eCT}	7 ± 1	7 ± 1	8 ± 2	10.2 ± 1.5	5 ± 1	8 ± 5	kV ⁻¹
α				-1.71 ± 0.07			—
δ^*				1.16 ± 0.01			—
$\chi^2/n.d.f$	4/5	3/6	1/5	13/13	11/6	2/5	—

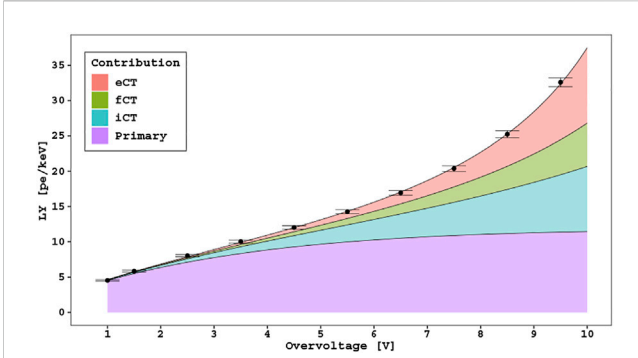


FIGURE 7
Breakdown of the CT components from the analytical model for the measured LY_G for the cubic chamber using ^{83m}Kr versus the over-voltage. Each band is estimated by zeroing the acceptances in Eq. 11, and therefore the eCT and fCT bands include a non-negligible fraction of iCT due to the detection of the corresponding cross-talk photons. The violet band (primary) accounts for the light yield at the specific over-voltage ($\bar{n}^{pe} \cdot P_{PDE}(V)$). The top black line represents the fit to the data using Eq. 11.

$$\mu(V) = \frac{1}{1 - (\lambda_{iCT}(V) + \lambda_{fCT}(V))} \quad (7)$$

which is valid only for $\lambda_{iCT} + \lambda_{fCT} \ll 1$.

Equation 8 represents the mean number of photo-electrons in the presence of iCT and fCT for an event of energy, E.

$$N^{pe}(V) = \bar{n}^{pe} \cdot E \cdot P_{PDE}(V) \cdot \mu(V), \quad (8)$$

where the parameter \bar{n}^{pe} indicates the asymptotic net light yield (which includes the scintillation yield of the argon, the chamber reflectivity, the TPB conversion efficiency, and the probability of materializing carriers outside the active region of the SiPM) and P_{PDE} is defined in Eq. 5.

With two SiPM arrays and in the presence of external cross-talk, we can define $\lambda_{eCT_{12}}$ ($\lambda_{eCT_{21}}$) as the number of avalanches in detector 2 (1) caused by a photo-electron in detector 1 (2). Equation 8 can be extended to

$$\begin{aligned} N_1^{pe}(V_1, V_2) &= \mu_1(V_1) \cdot (\bar{n}_1^{pe} \cdot E \cdot P_{PDE_1}(V_1) + N_2^{pe}(V_1, V_2) \cdot \lambda_{eCT_{21}}(V_2, V_1)), \\ N_2^{pe}(V_1, V_2) &= \mu_2(V_2) \cdot (\bar{n}_2^{pe} \cdot E \cdot P_{PDE_2}(V_2) + N_1^{pe}(V_1, V_2) \cdot \lambda_{eCT_{12}}(V_1, V_2)). \end{aligned} \quad (9)$$

Assuming a symmetric chamber with the same bias for both photo-detectors, Eq. 9 simplifies as if there was only a single photo-detector with $\lambda_{oCT} = \lambda_{iCT} + \lambda_{fCT} + \lambda_{eCT}$:

$$N_1^{pe}(V) = \frac{\bar{n}^{pe} / 2 \cdot E \cdot P_{PDE}(V)}{1 - \lambda_{oCT}(V)} = N_2^{pe}(V), \quad (10)$$

$$LY_G(V) = \frac{\bar{n}^{pe} \cdot P_{PDE}(V)}{1 - \lambda_{oCT}(V)}. \quad (11)$$

Equation 11 can be fit to the experimental data: it contains seven parameters: \bar{n}^{pe} , ζ , V_h , V_e , ξ_{iCT} , ξ_{fCT} , and ξ_{eCT} . V_h is set to the value obtained in Section 3.1, with a penalty in the chi-squared test. The fit to the data from the symmetric setup (equal tile biases) is only sensitive to λ_{oCT} and not to the individual components. We therefore set ξ_{iCT} and ξ_{fCT} to the values obtained in Section 3.1 and Section 3.3, respectively. The results of the minimization are

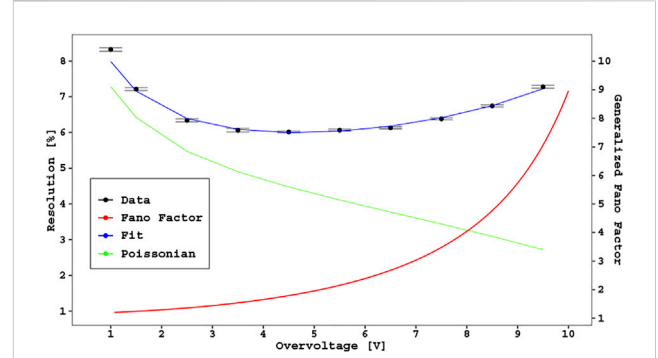


FIGURE 8
Energy resolution of the cubic chamber using ^{83m}Kr (data points in black). The solid blue line represents the prediction from the resolution fit (see text). The solid green line shows the pure Poissonian resolution, and the red line shows the calculated generalized Fano factor from Eq. 12 (relative to the axis scale on the right).

summarized in Table 1. Figure 7 shows the fit to the gross light yield with different colors indicating the different cross-talk contributions. Interestingly, at the over-voltage of above 7.7 V, the contribution from the optical cross-talk exceeds the number of primary photo-electrons.

3.5 Energy resolution

Another quantity of primary importance for particle detectors is the energy resolution. In our case, due to iCT, the resolution diverges from the Poissonian limit as described by a larger-than-unity generalized Fano factor, which is introduced in Section 3.1. The presence of fCT and eCT further increases this divergence. Analogous with Eq. 3, we define a global generalized Fano factor from cross-talk contributions as

$$\mathcal{F}_{oCT} = \delta^* \cdot (1 - \lambda_{oCT})^\alpha, \quad (12)$$

where α is the same as defined for the iCT only (Section 3.1). δ^* includes the contribution from the SiPMs, plus the spread introduced by the argon scintillation [25] and TPB wavelength shifter [26]. This results in

$$\frac{\sigma_G(E, V)}{E} = \sqrt{\frac{\mathcal{F}_{oCT}(V)}{E \cdot LY_G^{oV}}}, \quad (13)$$

which can be fit to the experimental data.

For the cubic chamber, with ^{83m}Kr , we obtain $\chi^2/n.d.f. = 12/7$ when fixing $V_h = 5.4$ V with a resulting ξ_{oCT} (the sum of the three CT acceptances) equal to $(78.0 \pm 0.3)/kV$ and $\delta^* = 1.157 \pm 0.006$. At the over-voltage of 1 V, the contribution of the electronic noise is dominant. We therefore exclude such a point from the fit. Figure 8 shows the experimental data and the fit prediction.

3.6 Global fit

We combine LY_G and the resolution fits into a global χ^2 with the goal of reducing the uncertainty on the results. We obtain

TABLE 2 Fraction of simulated photons absorbed by different detector components. Absorption by SiPMs represents the light collection efficiency of the system. Absorption by detector mechanics implies that the light escapes from the optical system of the detector.

Component	Fraction (%)
SiPM (collection efficiency)	70
Dead spaces in the SiPM tile	6
Reflectors and TPB	11
Detector mechanics (escape)	13

$$\frac{\sigma_G(E, V)}{E} = \sqrt{\frac{\mathcal{F}_{\text{oCT}}(V)}{E \cdot \text{LY}_G(V)}}, \quad (14)$$

where $\text{LY}_G(V)$ is predicted by the analytical model instead of the experimental data. The results of the χ^2 minimization of Eq. 14 are summarized in Table 1.

4 Optics

Dedicated Monte Carlo simulation software based on Geant4 [27] is developed, with the main focus on tracking the photons in the detectors under study. The simulation includes wavelength shifting, reflection, refraction, and absorption. Additionally, it incorporates the LAr scintillation process originating from particle interactions in LAr. The inner surface of the active LAr volume is almost entirely covered with TPB, and the wavelength-shifting efficiency of TPB is set to unity in the model.

A full model of the system is implemented, along with the surrounding LAr buffer and the detector geometry. Refractive indices, attenuation lengths, and surface properties of LAr, TPB, ESR foil, fused-silica windows, and SiPMs are included with adequate approximations. Some of these parameters were taken from the literature, and some were measured in dedicated setups. In particular, measurements of the wavelength-dependent reflectivity of the TPB-coated ESR foil (approximately 96%) and SiPM surface (approximately 17%) are reported in Ref. [12].

To estimate the light collection efficiency of the detector under study, 41.5 keV electrons are generated uniformly over the active volume, simulating the energy deposition from the $^{83\text{m}}\text{Kr}$ isotope. Table 2 summarizes the fraction of visible photons absorbed by different parts of the detector: the light collection is only affected by the fraction of light absorbed by the SiPM tiles. Figure 6 compares the simulated top-bottom asymmetry with the measured value.

Several issues arise when modeling the optics, the most important of which are: (1) the nature of the optical interface between the fused-silica window and TPB not being well understood and (2) the reflectivity of the SiPM, which has a multi-layer anti-reflective coating, is measured in air and projected to the LAr medium [12]. These issues affect the aforementioned light collection efficiency, and, hence, we estimate a systematic uncertainty of $\pm 5\%$ on its absolute value.

With the collection efficiency, it is possible to predict the LY of the system. Assuming that the PDE of the SiPM does not change by more than 10% with respect to the measurements at room

temperature [11] and 100% for the TPB VUV conversion efficiency [28], the optical model predicts a net light yield of 11.7 ± 1.3 photo-electrons/keV at the over-voltage of 6 V, which is in agreement with the value reported in Figure 7.

5 Conclusion

In this work, we parametrized the over-voltage dependence of optical cross-talk (oCT) in two small LAr chambers equipped with large SiPM arrays using an inclusive oCT model. The model involving internal (iCT) and external (fCT and eCT) components well describes the observed gross light yield and energy resolution, thus providing a plausible estimate of the contributions from primary photo-electrons and different cross-talk components. We obtain a net light yield value of up to 12 ± 1 photo-electrons/keV, which is one of the best light yield values obtained for an experimental setup using LAr. Despite the high net light yield, the oCT of the SiPMs becomes dominant above 7.7 V, significantly compromising the energy resolution of the detectors. Since SiPMs from any vendor are affected by external cross-talk, we recommend that previous results obtained using silicon readouts should be re-evaluated with a similar analysis.

Encouragingly, an effective parametrization of the oCT generation at cryogenic temperatures has been provided for the FBK NUV-HD-Cryo SiPMs. Even if the optical model of the chamber is tuned for the argon scintillation photons (in the UV/blue) and the optical cross-talk happens at longer wavelengths, we can use the collection efficiency as a first approximation to estimate the acceptances of fCT and eCT: $\xi_{\text{fCT}} + \xi_{\text{eCT}} \approx .6 \xi_{\text{iCT}}$. This implies that for every two photons trapped in the silicon bulk (candidates for iCT), one escapes through the front window.

Data availability statement

The raw data supporting the conclusion of this article will be made available by the authors, without undue reservation.

Author contributions

All authors listed have made a substantial, direct, and intellectual contribution to the work and approved it for publication. All authors contributed to the article and approved the submitted version.

Acknowledgments

The authors acknowledge support from the Istituto Nazionale di Fisica Nucleare (Italy) and Laboratori Nazionali del Gran Sasso (Italy) of INFN, from NSF (US, Grants PHY-1622415 and PHY-1812540 for Princeton University), from the Royal Society United Kingdom and the Science and Technology Facilities Council (STFC), part of the United Kingdom Research and Innovation, from the European Union's Horizon 2020 Research and Innovation Programme under grant agreement no. 952480 (DarkWave project), and from the International Research Agenda Programme AstroCeNT (MAB/2018/7) funded by the

Foundation for Polish Science (FNP) from the European Regional Development Fund.

Conflict of interest

The authors declare that the research was conducted in the absence of any commercial or financial relationships that could be construed as a potential conflict of interest.

References

- Newman R. Visible light from a silicon $p-n$ junction. *Phys Rev* (1955) 100:700–3. doi:10.1103/PhysRev.100.700
- Mirzoyan R, Kosyra R, Moser HG. Light emission in Si avalanches. *Nucl Instrum Methods Phys Res A* (2009) 610:98–100. doi:10.1016/j.nima.2009.05.081
- Nepomuk Otte A. On the efficiency of photon emission during electrical breakdown in silicon. *Nucl Instrum Methods Phys Res Sect A: Acc Spectrometers, Detectors Assoc Equip* (2009) 610:105–9. doi:10.1016/j.nima.2009.05.085
- Nagai A, Alispach C, Berghöfer T, Bonanno G, Coco V, della Volpe D, et al. Sense: A comparison of photon detection efficiency and optical crosstalk of various SiPM devices. *Nucl Instrum Methods Phys Res Sect A: Acc Spectrometers, Detectors Assoc Equip* (2018) 912:182–5. doi:10.1016/j.nima.2017.11.018
- McLaughlin JB, Gallina G, Retière F, De St Croix A, Giampa P, Mahtab M, et al. Characterisation of SiPM photon emission in the dark. *Sensors* (2021) 21:5947. doi:10.3390/s21175947
- Agostini M, Altenmüller K, Appel S, Atroshchenko V, Bagdasarian Z, Basilico D, et al. Comprehensive measurement of pp -chain solar neutrinos. *Nature* (2018) 562:505–10. doi:10.1038/s41586-018-0624-y
- Richard E, Okumura K, Abe K, Haga Y, Hayato Y, Ikeda M, et al. Measurements of the atmospheric neutrino flux by super-kamiokande: Energy spectra, geomagnetic effects, and solar modulation. *Phys Rev D* (2016) 94:052001. doi:10.1103/PhysRevD.94.052001
- Amerio S, Amoroso S, Antonello M, Aprili P, Armenante M, Arneodo F, et al. Design, construction and tests of the ICARUS T600 detector. *Nucl Instrum Meth A* (2004) 527:329–410. doi:10.1016/j.nima.2004.02.044
- Abi B, Acciarri R, Acero MA, Adamov G, Adams D, Adinolfi M, et al. Prospects for beyond the standard model physics searches at the deep underground neutrino experiment. *Eur Phys J C* (2021) 81:322. doi:10.1140/epjc/s10052-021-09007-w
- Ajaj R, Amaudruz PA, Araujo GR, Baldwin M, Batygov M, Beltran B, et al. Search for dark matter with a 231-day exposure of liquid argon using DEAP-3600 at SNOLAB. *Phys Rev D* (2019) 100:022004. doi:10.1103/PhysRevD.100.022004
- Aalseth CE, Acerbi F, Agnes P, Albuquerque IFM, Alexander T, Alici A, et al. DarkSide-20k: A 20 tonne two-phase LAr TPC for direct dark matter detection at LNGS. *Eur Phys J Plus* (2018) 133:131. doi:10.1140/epjp/i2018-11973-4
- Boulay MG, Camillo V, Canci N, Choudhary S, Consiglio L, Flammini A, et al. Direct comparison of PEN and TPB wavelength shifters in a liquid argon detector. *Eur Phys J C* (2021) 81:1099. doi:10.1140/epjc/s10052-021-09870-7
- Agnes P, Alexander T, Alton A, Arisaka K, Back H, Baldin B, et al. First results from the DarkSide-50 dark matter experiment at Laboratori Nazionali del Gran Sasso. *Phys Lett B* (2015) 743:456–66. doi:10.1016/j.physletb.2015.03.012
- Kochanek I. Packaging strategies for large SiPM-based cryogenic photo-detectors. *Nucl Instrum Methods Phys Res A* (2020) 980:164487. doi:10.1016/j.nima.2020.164487
- Gola A, Acerbi F, Capasso M, Marcante M, Mazzi A, Paternoster G, et al. NUV-sensitive silicon photomultiplier technologies developed at Fondazione Bruno Kessler. *Sensors* (2019) 19:308. doi:10.3390/s19020308

Publisher's note

All claims expressed in this article are solely those of the authors and do not necessarily represent those of their affiliated organizations, or those of the publisher, the editors, and the reviewers. Any product that may be evaluated in this article, or claim that may be made by its manufacturer, is not guaranteed or endorsed by the publisher.

- D'Incecco M, Galbiati C, Giovanetti GK, Korga G, Li X, Mandarano A, et al. Development of a novel single-channel, 24 cm², SiPM-based, cryogenic photodetector. *IEEE Trans Nucl Sci* (2018) 65:591–6. doi:10.1109/TNS.2017.2774779
- Adhikari P, Ajaj R, Araujo G, Batygov R, Beltran B, Bina C, et al. The liquid-argon scintillation pulse shape in DEAP-3600. *Eur Phys J C* (2020) 80:303. doi:10.1140/epjc/s10052-020-7789-x
- Vinogradov S, Vinogradova T, Shubin V, Shushakov D, Sitarsky K. Probability distribution and noise factor of solid state photomultiplier signals with cross-talk and afterpulsing. In: 2009 IEEE Nuclear Science Symposium Conference Record (NSS/MIC) (2009). p. 1496–500. doi:10.1109/NSSMIC.2009.5402300
- Nagai A, Alispach C, Barbano A, Coco V, della Volpe D, Heller M, et al. Characterization of a large area silicon photomultiplier. *Nucl Instrum Methods Phys Res Section A: Acc Spectrometers, Detectors Associated Equipment* (2019) 948:162796. doi:10.1016/j.nima.2019.162796
- McIntyre RJ. Theory of microplasma instability in silicon. *J Appl Phys* (1961) 32:983–95. doi:10.1063/1.1736199
- Otte ANO, Garcia D, Nguyen T, Purushotham D. Characterization of three high efficiency and blue sensitive silicon photomultipliers. *Nucl Instrum Methods Phys Res Section A: Acc Spectrometers, Detectors Assoc Equip* (2017) 846:106–25. doi:10.1016/j.nima.2016.09.053
- Zappalà G, Acerbi F, Ferri A, Gola A, Paternoster G, Regazzoni V, et al. Study of the photo-detection efficiency of FBK high-density silicon photomultipliers. *J Instrum* (2016) 11:P11010. doi:10.1088/1748-0221/11/11/p11010
- Dinu N, Nagai A, Para A. Breakdown voltage and triggering probability of SiPM from IV curves at different temperatures. *Nucl Instrum Methods Phys Res Section A: Acc Spectrometers, Detectors Assoc Equip* (2017) 845:64–8. doi:10.1016/j.nima.2016.05.110
- Vinogradov S. Analytical models of probability distribution and excess noise factor of solid state photomultiplier signals with crosstalk. *Nucl Instrum Methods Phys Res A* (2012) 695:247–51. doi:10.1016/j.nima.2011.11.086
- Doke T, Hitachi A, Kubota S, Nakamoto A, Takahashi T. Estimation of Fano factors in liquid argon, krypton, xenon and xenon-doped liquid argon. *Nucl Instrum Methods* (1976) 134:353–7. doi:10.1016/0029-554X(76)90292-5
- Francini R, Montecchi RM, Nichelatti E, Vincenti MA, Canci N, Segreto E, et al. VUV-Vis optical characterization of tetraphenyl-butadiene films on glass and specular reflector substrates from room to liquid argon temperature. *J Instrum* (2013) 8:P09006. doi:10.1088/1748-0221/8/09/p09006
- Allison J, Amako K, Apostolakis J, Arce P, Asai M, Aso T, et al. Recent developments in Geant4. *Nucl Instrum Methods Phys Res A* (2016) 835:186–225. doi:10.1016/j.nima.2016.06.125
- Kuźniak M, Szalc AM. Wavelength shifters for applications in liquid argon detectors. *Instruments* (2021) 5:4. doi:10.3390/instruments5010004